

Rapidly immobilization of simulated $An3+$ radioactive contaminated soil as glass-ceramics by microwave sintering

Fen Luo

Southwest University of Science and Technology

Haojie Tan

Southwest University of Science and Technology

Xiaoyan Shu

Southwest University of Science and Technology

Yulong Miao

Southwest University of Science and Technology

Shunzhang Chen

Sichuan University

Beilong Yuan

Southwest University of Science and Technology

Lan Wang

University of Science and Technology of China

Yi Xie

University of Science and Technology of China

Xirui Lu (✉ luxiruimvp116@163.com)

Southwest University of Science and Technology <https://orcid.org/0000-0003-4751-8408>

Research Article

Keywords: Solubility, Simulated $An3+$, Microwave sintering, Immobilization

Posted Date: October 8th, 2020

DOI: <https://doi.org/10.21203/rs.3.rs-86505/v1>

License:   This work is licensed under a Creative Commons Attribution 4.0 International License.

[Read Full License](#)

Abstract

The development of nuclear technology leads to the generation of radionuclide contaminated soils, which require efficient and rapid disposal methods. In this study, with microwave sintering method, the simulated radionuclides contaminated soils were successfully immobilized as glass-ceramics at 1200 °C with 30 min. The temperature effect, phase evolution, morphology, element distribution of simulated radioactive contaminated soil were investigated. The XRD results showed that Nd 3+ were immobilized into glass-ceramic phases with Nd 2 O 3 content increased up to 25 wt %. In addition, molecular dynamics simulation (MD) results showed the simulated radioactive contaminated soils were composed of [SiO 4] tetrahedron, and Si-O-Si bonds had an important effects on the glass structure forming.

1. Introduction

With the development and application of nuclear technology, nuclear energy has played an important role in energy field [1]. In the process of utilizing nuclear energy, the public health is threatened by the release of harmful radionuclides [2]. Especially after Fukushima Daiichi Accident, the effective treatment and management of harmful radionuclides become a topic of global concern [3]. Radionuclide contaminated soils are originated from the uranium mining, nuclear facility operation, nuclear decommissioning and nuclear tests, which pose a great threat to human health [4]. Therefore, it is a challenging task to safely disposal of radionuclide contaminated soils.

In situ vitrification (ISV) technology is a commonly effective method of remediation contaminated soils [5]. Early in the 1980s, ISV technology by joule heating has been developed by the Pacific Northwest Laboratory of the US, and then applied to the disposal of contaminated soils in Maralinga nuclear test site of the UK [6]. In the process of joule heating, the materials are heated to melting through high power currents, and then cooled with rapid speed. The traditional joule heating method requires the long heating time, and the uniformity of the solidification is difficult to obtain [7]. Due to the advantages of homogeneous heating and remediation time reducing, microwave sintering technique has been applied in the field of remediation contaminated soils [8, 9]. The microwave sintering technique can convert absorb microwave energy into heat energy, and the materials are heated at the same time [10].

To explore the effective methods of remediation contaminated soils, many scientists have devoted to microwave sintering technique [11–18]. Jou [15] have reported that the Pb polluted soils are successfully immobilized by microwave sintering technique, with a low Pb leaching concentration. The hydrocarbon contaminated soils have been remediated through the microwave sintering technique, and the impact factors of microwave power and moisture content have been investigated [16]. In our previous work, Ce-doped simulated radionuclides contaminated soils [17] and uranium-contaminated soils [18] have been vitrified with microwave sintering. Therefore, it can be inferred that the microwave sintering technique is an effective method to treat the contaminated soils. However, few works have been reported on the immobilization mechanism through the combined with experimental and theoretical methods.

In this work, simulated radionuclides contaminated soils were investigated by the experimental and theoretical methods. A series of simulated radionuclides contaminated soils were immobilized by microwave sintering at different temperatures. Nd_2O_3 was considered to be a simulated radionuclides of An^{3+} (such as Am^{3+} , Pu^{3+} , Cm^{3+}), owing to the same valence and similar ionic radius ($R_{\text{Nd}^{3+}} = 1.11 \text{ \AA}$, $R_{\text{Am}^{3+}} = 1.01 \text{ \AA}$, $R_{\text{Pu}^{3+}} = 1.00 \text{ \AA}$ and $R_{\text{Cm}^{3+}} = 0.97 \text{ \AA}$) [19]. The phase evolution, morphology and element distribution of sintered samples are collected by using the experimental method. Molecular dynamics simulations were employed to exploring the structure information of simulated radionuclides contaminated soils.

2. Methods

2.1. Fabrication

The pristine soil composition was listed in Table 1, which was measured by XRF (Axios, Netherlands). To remove adsorptive water, the soil (200 mesh) and Nd_2O_3 powder (Tianjin Kermel Co. Ltd., purity $\geq 99.99\%$) were preheated at $100 \text{ }^\circ\text{C}$ for 12 h. Four kinds of Nd_2O_3 addition contents were selected as 10 wt %, 15 wt %, 20 wt % and 25 wt %, respectively. The mixed soil samples were weighed at 5.0 g. Then, the pristine soil and the Nd_2O_3 powder were sufficiently mixed in a mortar by grinding with ethyl alcohol (AR grade) until the mixed powder dried absolutely. All mixed soil samples were sintered by microwave sintering furnace (HAMiLab-M1500) at $1000 \text{ }^\circ\text{C}$ – $1100 \text{ }^\circ\text{C}$ and $1200 \text{ }^\circ\text{C}$ for 30 min. The samples were heated at the rate of $30 \text{ }^\circ\text{C}/\text{min}$, and then cooled down to room temperature.

Table 1 Composition of the pristine soil.

	SiO_2	Al_2O_3	CaO	Fe_2O_3	MgO	K_2O	Na_2O	TiO_2
Content (wt %)	66.32	16.57	4.67	5.87	1.66	2.86	0.81	0.74

2.2. Characterization

To confirm the phase structure of samples, X-ray diffraction (XRD, X'Per PRO, Netherlands) was used with Cu $K\alpha$ radiation ($\lambda = 1.5406 \text{ \AA}$). The scanning ranged from 10° to 80° with the scanning rate of $8^\circ/\text{min}$. In addition, Fourier Transform Infrared Spectroscopy (FT-IR, PE, Spectrum One) was employed to obtain the detailed structure information. The micro-morphology and element distribution of samples were analyzed by using Scanning Electron Microscope (SEM, TM-4000, Hitachi) and energy dispersive spectrometry (EDS), respectively.

2.3. Computational methods

In MD simulations, the General Utility Lattice Program (GULP) code [20] was chosen to analyze the micro-structure of system. The 25 wt % Nd_2O_3 doped soil was selected. The Buckingham potential was employed to describe the inter-atom interaction, which can be expressed as follow [21]

$$U_{ij}(r_{ij}) = \frac{z_i z_j}{r_{ij}} + A_{ij} \exp\left(\frac{-r_{ij}}{\rho_{ij}}\right) - \frac{C_{ij}}{r_{ij}^6} \quad (1)$$

where r_{ij} is the distance between atoms i and j , Z_i and Z_j are the effective charges of atoms i and j , A_{ij} , ρ_{ij} and C_{ij} are the parameters of atom i - j interaction. The related parameters [21, 22] of Buckingham potential were shown in Table 2.

Table 2 Parameters of the inter-atomic interaction potential.

	A_{ij} (eV)	ρ_{ij} (Å)	C_{ij} (eV·Å ⁶)
O-O	9022.82	0.265	85.0924
Al-O	28538.48	0.172	34.5779
Si-O	50306.25	0.161	46.2979
Ca-O	155668.01	0.178	42.2598
Fe-O	8020.29	0.19	0.0000
Mg-O	32652.71	0.178	27.2810
K-O	2284.78	0.29	0.0000
Na-O	120304.17	0.17	0.0000
Ti-O	50126.74	0.178	46.2979
Nd-O	13084.217	0.255	0.0000

Around 2100 atoms were distributed randomly in simulations box, which were used as the initial modes of MD simulations. The 11 Å cutoff distance and 1 fs time step were applied in the whole simulations process. At first, the canonical (NVT) ensemble was employed to heat the randomly distributed atoms to 5000 K for 100 ps. Then the systems were cooled to 300 K with the 5 K/ps cooling speed, and the NVT ensemble was applied in the cooling process. Lastly, at 300 K, the systems were reduced the inner stress with the microcanonical (NVE) ensemble for 100 ps, and the related trajectory data were collected by the final 800 configurations for structural analysis.

3. Result And Discussion

3.1 XRD analysis

In order to investigate the structure information of samples, the XRD patterns of the simulated radioactive waste samples are sintered at 1000 °C, 1100 °C and 1200 °C, which are shown in Fig. 1. Figure 1 (a) shows that the main peaks of sintered samples are SiO₂ and Ca₂SiO₄ with the 10 wt % Nd₂O₃ content.

When the amounts of Nd_2O_3 range from 20 wt % to 25 wt %, the peaks of Ca_2SiO_4 disappear, and the peaks of Mg_2SiO_4 and $\text{Ca}_3\text{Mg}(\text{SiO}_4)_2$ appear. This suggested that Ca_2SiO_4 is related to the forming of Mg_2SiO_4 and $\text{Ca}_3\text{Mg}(\text{SiO}_4)_2$. With the Nd_2O_3 content increasing, the intensity of SiO_2 peaks increases. As shown in Fig. 1 (b), it can be seen that the peaks of $\text{NaCaAlSi}_2\text{O}_7$ disappear and the peaks of Mg_2SiO_4 , $\text{Ca}_3\text{Mg}(\text{SiO}_4)_2$ and amorphous phase appear until the Nd_2O_3 content increases up to 15 wt %. The intensity of SiO_2 peak increases with the increasing of Nd_2O_3 content. The XRD results of samples with 10–25 wt. % Nd_2O_3 concentrations at 1200 °C are shown in Fig. 1 (c). It is shown that the crystal peak of SiO_2 and the amorphous characteristic are detected when the amounts of Nd_2O_3 are in the range of 10 wt % to 25 wt %. As the Nd_2O_3 content increase, the main peaks of SiO_2 increase, and the peaks of Mg_2SiO_4 and $\text{Ca}_3\text{Mg}(\text{SiO}_4)_2$ appear.

Figure 1 (d) shows that the XRD results of samples with the doped contents of 25 wt. % Nd_2O_3 at different temperatures. When temperature varies from 1000 °C to 1200 °C, the main peaks of SiO_2 , Mg_2SiO_4 and $\text{Ca}_3\text{Mg}(\text{SiO}_4)_2$ are detected, and the peaks of amorphous phase at $2\theta = 20^\circ - 30^\circ$ are observed, indicating that the glass-ceramic phases appear in sintered soil samples. With the increase of temperature, the crystal diffraction peaks of SiO_2 , Mg_2SiO_4 and $\text{Ca}_3\text{Mg}(\text{SiO}_4)_2$ decrease, and peaks of amorphous phase become distinct. It can be deduced that the glass forming ability increases at elevated temperature. In addition, the XRD results show no obvious crystal peaks of the related Nd compounds are observed with the doped content of 25 wt % Nd_2O_3 , indicating that Nd^{3+} are immobilized into glass-ceramic phases.

3.2 Morphology analysis

Figure 2 shows the macro-morphology of simulated radioactive contaminated samples before and after sintering. The results show that the volumes of samples reduce after sintering, which are benefit to the transportation process and geological disposal [23, 24]. The sample of No.8 has a rough surface, and the samples of No. 12 and 16 have smooth and lustrous surfaces.

The SEM and corresponding element mapping images of sintered samples are investigated to observe the micro morphology of samples, which are presented in Fig. 3. The SEM results reveal that the holes exists in the sample surface at 1000 °C, while smooth surfaces are observed in the samples at 1100 °C and 1200 °C. Furthermore, Fig. 3 (d) - (f) show that the Nd elements present uniform distribution without enrichment phenomenon with the doped amount of 25 wt %.

3.3 FT-IR analysis

The detailed structure information of sintered samples has been measured by FT-IR for confirming the existing form of neodymium. Figure 4 shows the FT-IR spectra of sintered samples with 10–25 wt % doped content of Nd_2O_3 at different temperatures. The range of main absorption peaks are located between 400 cm^{-1} and 2000 cm^{-1} . From Fig. 4 (a) to 4 (c), it can be seen that the absorption bands are

located at around 1627 cm^{-1} and 1633 cm^{-1} , which are assigned to H-O-H bonds [25]. In addition, weak flexural vibration peaks of 1384 cm^{-1} are attributed to the $-\text{CH}_3$ bonds, which may be attributed to the residual alcohol in the process of preparing samples [26]. The strong and wide absorption peaks appear in the range of 850 cm^{-1} to 1300 cm^{-1} , which are related to the anti-symmetric stretching vibration peaks of Si-O-Si bonds [27]. The characteristic bending vibrations ranging from 760 cm^{-1} to 850 cm^{-1} and at 467 cm^{-1} are caused by Si-O bonds [28]. Figure 4 (d) shows that the intensity of Si-O-Si bonds increase with the increase of temperature. The temperature has little effect on the intensity of H-O-H and $-\text{CH}_3$ bonds. Moreover, the FT-IR results show that no related Nd bonds are observed in all samples. Combining with the results of XRD and SEM, it can be inferred that the Nd has been solidified in the soil matrix.

According to the above discussed, the sintered samples mainly consist of the Si-O-Si bonds. To investigate the network structure of sintered samples, the numbers of bridging oxygen bonds (BO) and non-bridging oxygen bonds (NBO) are studied, which can be represented by the Q_n (n is the number of bridging oxygen bonds) species of Si-O tetrahedron. Generally, the FT-IR bands at about 870 cm^{-1} , 920 cm^{-1} , 990 cm^{-1} , 1090 cm^{-1} and 1200 cm^{-1} are assigned to the Q_0 , Q_1 , Q_2 , Q_3 and Q_4 , respectively [29]. Figure 5 shows the Q_n species of 25 wt % Nd_2O_3 doped soils at different temperature. It is shown that the network connectivity of sintered samples is affected by the temperature, and the non-bridging oxygen bonds translate into the bridging oxygen bonds. At $1000\text{ }^\circ\text{C}$, the Q_2 , Q_3 and Q_4 are 29.31%, 44.07% and 26.62%, respectively. As the temperature increases, the numbers of Q_2 decrease, indicating that the numbers of NBO decrease in sintered samples. The numbers of $Q_3 + Q_4$ increase with the increase of temperature, which can explain that the temperature improves the intensity of Si-O-Si bonds. The sintered sample at $1200\text{ }^\circ\text{C}$ has more than 75% of Si-O tetrahedrons with three and four BO, indicating that the glass network structure becomes stability. The structure information will be discussed by the following MD simulation results.

3.4 Structure analysis with MD simulations

MD simulations are applied to the system with 2100 atoms, and the structure corresponds to 25 wt % Nd_2O_3 doped sintered soils, which is performed with the following molar ratio: 74.53 mol % SiO_2 , 10.95 mol % Al_2O_3 , 2.47 mol % Fe_2O_3 , 5.62 mol % CaO , 2.05 mol % K_2O , 2.8 mol % MgO , 0.88 mol % Na_2O , 0.62 mol % TiO_2 and 0.07 mol % Nd_2O_3 , as shown in Fig. 6. It is shown that Nd distributes uniform in our simulated sintered soils, which agrees with the experimental results.

Figure 7 shows the simulated radial distribution function (RDF) for 25 wt % Nd_2O_3 doped sintered soils. Generally, the bond length can be deduced by the first peak position of RDF [30]. The bond length of Si-O is 1.62 \AA in simulated soils, which is close to the experimental values of 1.61 \AA [31]. The bond length of Al-O is 1.75 \AA , which is consistent with the experimental results of Extended X-ray absorption fine structure (EXAFS) [32]. Our simulated results agree well with the experimental results, indicating that the simulated method is reasonable. The order of bond length is $\text{Si-O} < \text{Al-O} < \text{Fe-O} < \text{Ti-O} < \text{Mg-O} < \text{Ca-O} < \text{Na-O}$

< Nd-O < K-O, which is presented in Fig. 7. It can be assumed that Al and Si atoms are close to O atoms. As shown in Fig. 7, the first peaks of Si-O are narrow and sharp, whereas the first peaks of Nd-O are broad and low intensity. It is implied that the bonding ability of Si-O is strongest in all bonds. From above Q_n species analysis, it is shown that the numbers of $[\text{SiO}_4]$ increase as the temperature increases. It can be concluded that the Si-O bonds play an important role in forming glass ability.

Simulated bond angle distributions for 25 wt% Nd_2O_3 doped sintered soils are shown in Fig. 8. It is shown that the bond angles of O-Si-O and Si-O-Si are around 105° and 136° , which indicates $[\text{SiO}_4]$ tetrahedron exists in our simulated sintered soils. It is consistent with the Q_n results that more than 75% of Si-O tetrahedrons with three and four BO. With high energy X-ray diffraction, Poulsen *et al* [32] investigated that the bond angles of O-Si-O and Si-O-Si are around 109° and 147° , respectively. The main peak of O-Al-O bond angle distributions is around 104° , which is lower than that of O-Si-O. The O-Al-O bond angle distributions have two apparent peaks: one main peak at around 117° and the other small peak at around 91° .

4. Conclusion

In summary, the simulated radionuclides contaminated soils were rapidly immobilized as glass-ceramics material by microwave sintering at 1200°C with 30 min. With the increasing of temperature, the crystal diffraction peaks decreased, and the diffraction peaks of amorphous phase increased, indicating that the glass forming ability increased at elevated temperature. Nd^{3+} were immobilized into glass-ceramics structure with the Nd_2O_3 doped content increases up to 25 wt%. The SEM results showed that Nd element distributed uniform in the soil matrix. Experimental and theoretical results showed that the sintered soil samples were mainly composed of $[\text{SiO}_4]$ tetrahedron, which will affect the stability of glass network structure. The microwave sintering has been posed to be a potential method for rapidly and effectively disposing of radionuclides contaminated soils.

Declarations

Acknowledgements

The authors would like to thank financial supports from Key Laboratory of Eco-geochemistry, Ministry of Natural Resources, (No.ZSDHJJ201903), National Natural Science Foundation of China (No.21677118).

References

1. Dai J, Li S, Bi J et al (2019) The health risk-benefit feasibility of nuclear power development. *J Clean Prod* 224:198–206
2. Turconi R, Boldrin A, Astrup T (2013) Life cycle assessment (LCA) of electricity generation technologies: overview, comparability and limitations. *Renew Sustain Energy Rev* 28:555–565

3. Zhang Z, Ninomiya K, Yamaguchi Y et al (2018) Atmospheric Activity Concentration of ^{90}Sr and ^{137}Cs after the Fukushima Daiichi Nuclear Accident. *Environ Sci Technol* 52:17–9925
4. Santos-Francés F, Pacheco E, Martínez-Graña A et al (2018) Concentration of uranium in the soils of the west of Spain. *Environ Pollut* 236:1–11
5. Guo G, Zhou Q, Ma L (2006) Availability and Assessment of Fixing Additives for the In Situ Remediation of Heavy Metal Contaminated Soils: A Review, *Environ. Monit Assess* 116:513–528
6. Buelte JL, Bonner WF, In Situ Vitrification: Test Results for a Contaminated Soil Melting process, Pacific Northwest Lab., Richland, WA (United States), 1989
7. Dixon DR, Schweiger MJ, Riley BJ et al (2015) Temperature distribution within a cold cap during nuclear waste vitrification. *Environ Sci Technol* 49:8856–8863
8. Jones DA, Lelyveld TP, Mavrofidis SD et al (2002) Microwave heating applications in environmental engineering – a review. *Resour Conserv Recycl* 34:75–90
9. Brosnan KH, Messing GL, Agrawal DK (2003) Microwave sintering of alumina at 2.45 GHz. *J Am Ceram Soc* 86:1307–1312
10. Robinson JP, Kingman SW, Snape CE et al (2009) Separation of polyaromatic hydrocarbons from contaminated soils using microwave heating. *Sep Purif Technol* 69:249–254
11. Kawala Z, Atamańczuk T (1998) Microwave-enhanced Thermal Decontamination of Soil. *Environ Sci Technol* 32:2602–2607
12. Li D, Zhang Y, Quan X et al (2009) Microwave thermal remediation of crude oil contaminated soil enhanced by carbon fiber. *J Environ Sci* 21:1290–1295
13. Mutyala S, Fairbridge C, Paré JRJ et al (2010) Microwave applications to oil sands and petroleum: a review. *Fuel Process Technol* 91:127–135
14. Yuan S, Tian M, Lu X (2006) Microwave remediation of soil contaminated with hexachlorobenzene. *J Hazard Mater* 137:878–885
15. Jou CJG (2006) An efficient technology to treat heavy metal–lead–contaminated soil by microwave radiation. *J Environ Manag* 78:1–4
16. Sivagamia K, Padmanabhanb K, Joy AC et al (2019) Microwave (MW) remediation of hydrocarbon contaminated soil using spent graphite – An approach for waste as a resource. *J Environ Manag* 230:151–158
17. Shu X, Chen S, Huang W, Immobilization of simulated An^{4+} in radioactive contaminated clay via microwave sintering (2020) *Mater Chem Phys* 254:123534
18. Shu X, Li Y, Huang W (2020) Rapid vitrification of uranium-contaminated soil: Effect and mechanism. *Environ Pollut* 263:114539
19. Lutique S, Staicu D, Konings RJM et al (2003) Zirconate pyrochlore as a transmutation target: thermal behaviour and radiation resistance against fission fragment impact. *J Nucl Mater* 319:59–64
20. Gale JD, Rohl AL (2003) The General Utility Lattice Program (GULP). *Mol Simul* 29:291–341

21. Guillot B, Sator N (2007) A Computer Simulation Study of Natural Silicate Melts. Part II: High Pressure Properties. *Geochim Cosmochim Acta* 71:4538–4556
22. Bush TS, Gale JD, Catlow CRA et al (1994) Self-consistent interatomic potentials for the simulation of binary and ternary oxides. *J Mater Chem* 4:831–837
23. Ojovan MI, Lee WE (2011) Glassy wastefoms for nuclear waste immobilization. *Metall Mater Trans A* 42:837–851
24. Jin BP, Jung H, Lee EY et al (2009) Wolsong low- and intermediate-level radioactive waste disposal center. *Nucl Eng Technol* 41:1–16
25. Dulina NA, Yermolayeva YV, Tolmachev AV et al (2010) Synthesis and characterization of the crystalline powders on the basis of Lu_2O_3 : Eu^{3+} spherical submicron-sized particles. *J Eur Ceram Soc* 30:1717–1724
26. Dhivya Prabha R, Santhanalakshmi J, Arun Prasath R (2013) Analysis of micellar behavior of as synthesized sodium itaconate monoesters with various hydrophobic chain lengths, in aqueous media. *Res J Chem Sci* 3:43–49
27. Chen H, Sun Z, Shao J (2011) Investigation on FT-IR spectroscopy for eight different sources of SiO_2 . *Bull Chin Ceram Soc* 30:934–937
28. Stefanovsky SV, Stefanovsky OI, Kadyko MI (2016) FTIR and Raman spectroscopic study of sodium aluminophosphate and sodium aluminum-iron phosphate glasses containing uranium oxides. *J Non-Cryst Solids* 443:192–198
29. Park JH, Min DJ, Song HS (2002) FT-IR Spectroscopic Study on Structure of CaO-SiO_2 and $\text{CaO-SiO}_2\text{-CaF}_2$ Slags. *ISIJ Int* 42:344–351
30. Lu X, Deng L, Du J (2018) Effect of ZrO_2 on the structure and properties of soda-lime silicate glasses from molecular dynamics simulations. *J Non-Cryst Solids* 491:141–150
31. Greaves GN, Fontaine A, Lagarde P et al (1981) Local structure of silicate glasses. *Nature* 293:611–616
32. Mckeown DA, Waychunas GA, Jr GEB (1985) EXAFS study of the coordination environment of aluminum in a series of silica-rich glasses and selected minerals within the $\text{Na}_2\text{O-Al}_2\text{O}_3\text{-SiO}_2$ system. *J Non-Cryst Solids* 74:349–371
33. Poulsen HF, Neufelnd J, Neumann H-B et al (1995) Amorphous silica studied by high energy X-ray diffraction. *J Non-Cryst Solids* 188:63–74

Figures

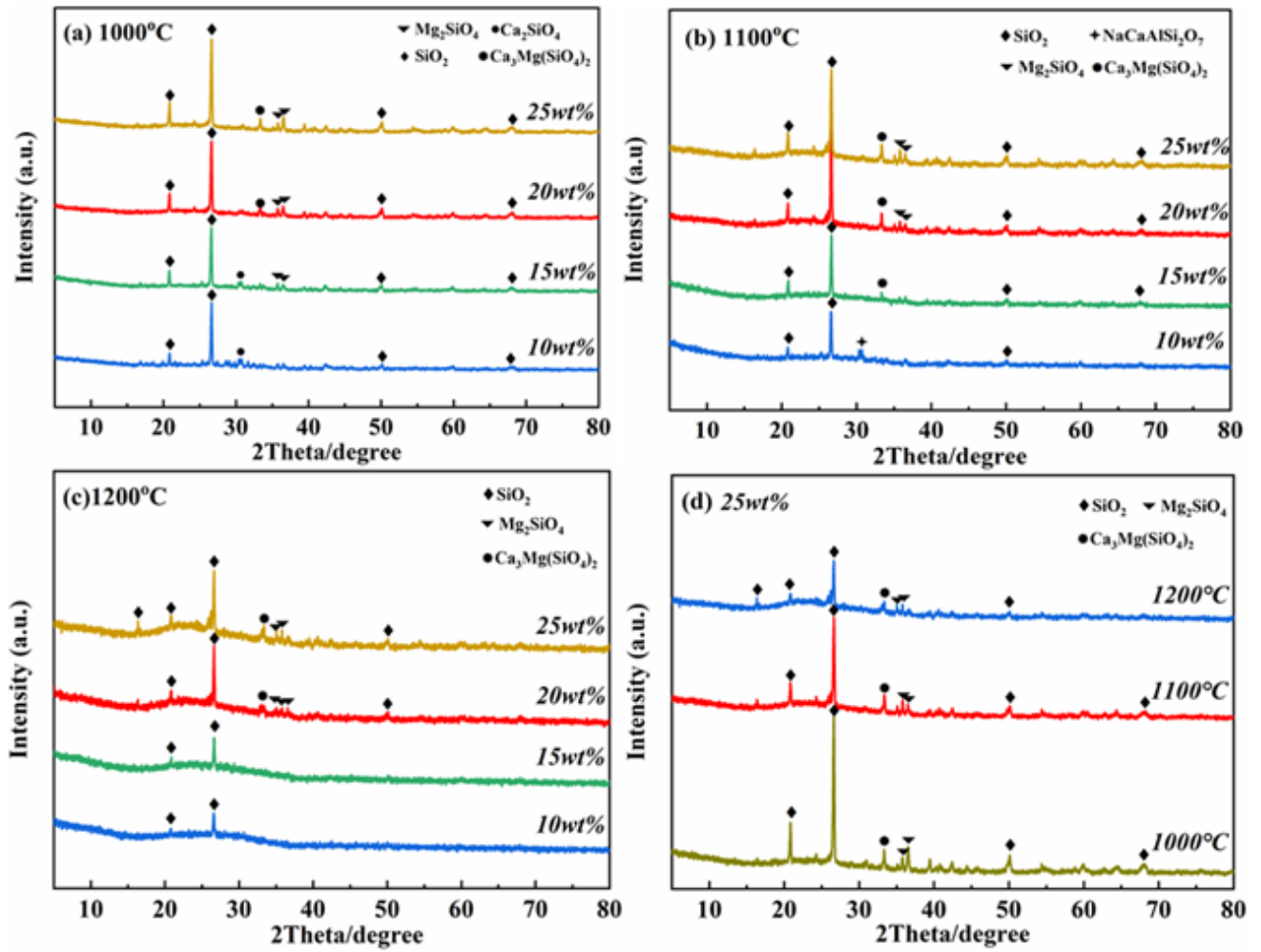


Figure 1

XRD patterns of samples with 10 - 25 wt % Nd₂O₃ concentrations at different temperatures

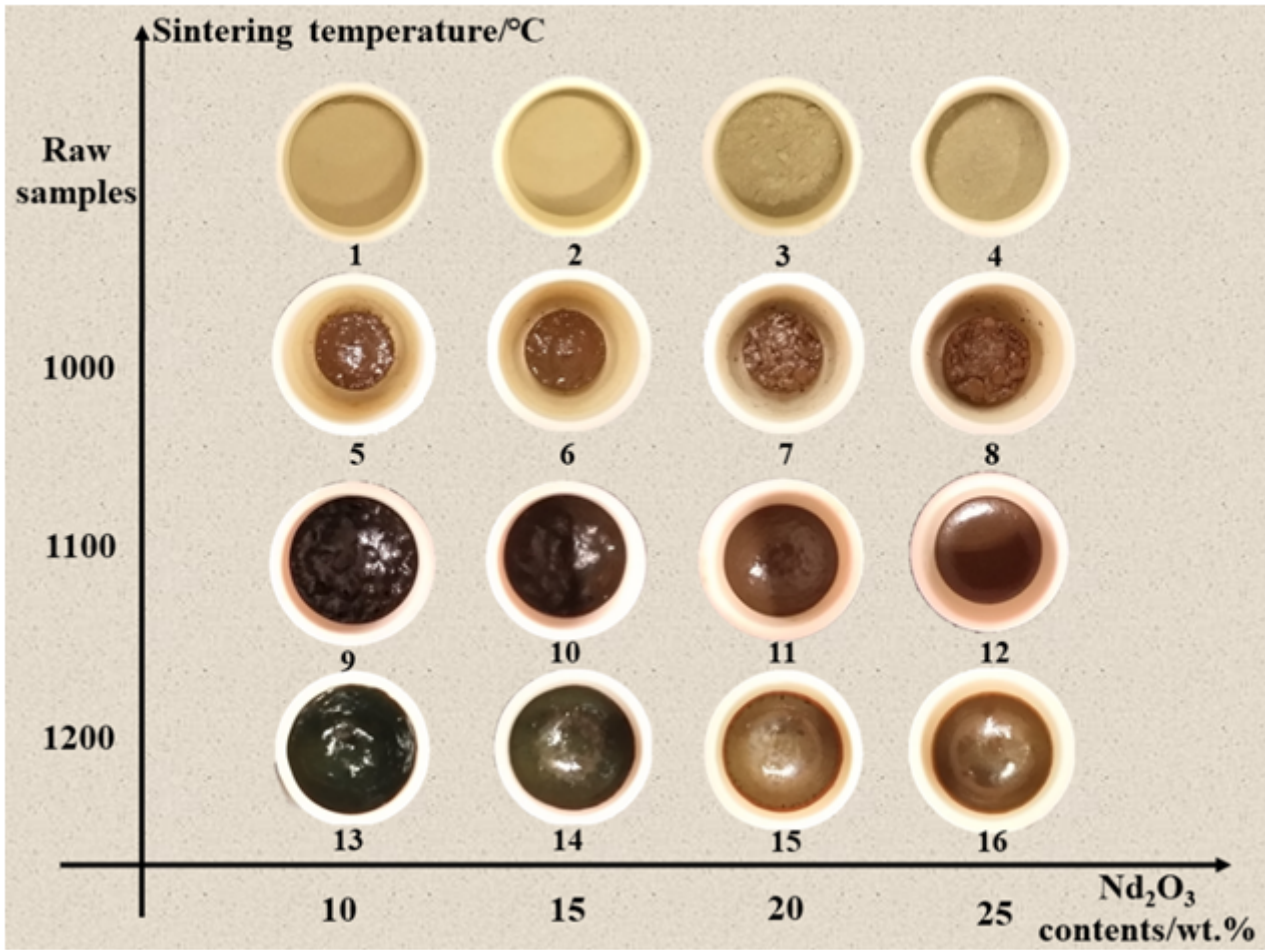


Figure 2

Pictures of simulated radioactive contaminated samples before sintering (No. 1 - 4) and after sintering (No.5 - 16)

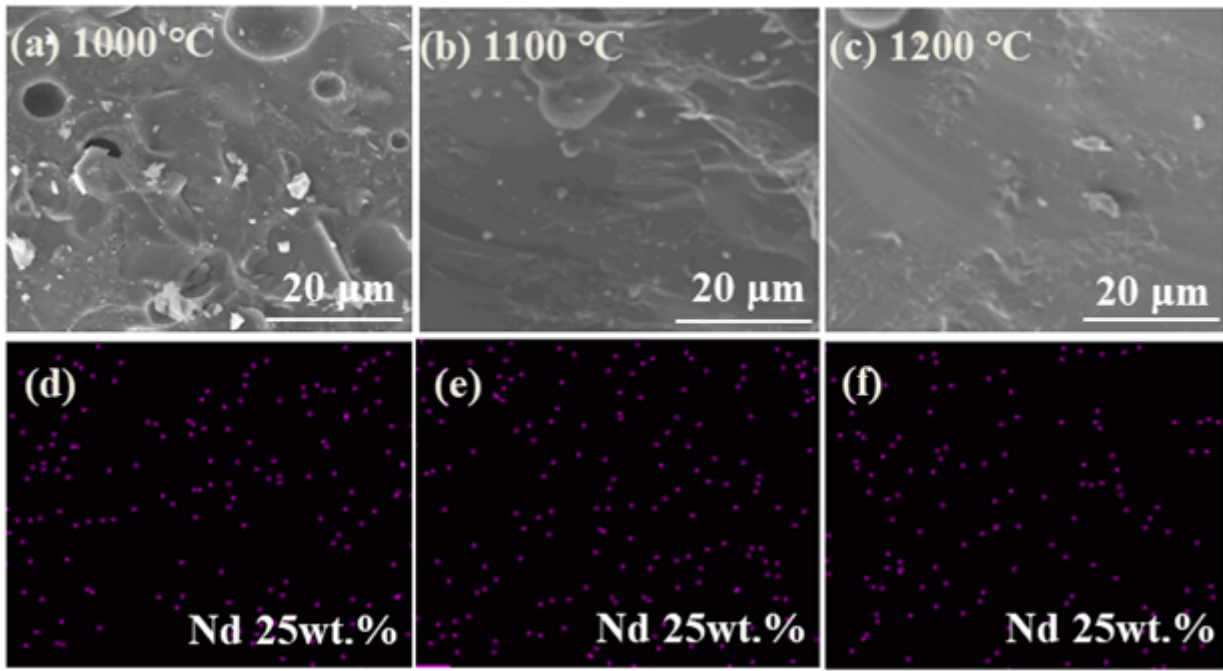


Figure 3

SEM image and corresponding element mapping image of sintered samples with the Nd₂O₃ doping content of 25 wt % at different temperature

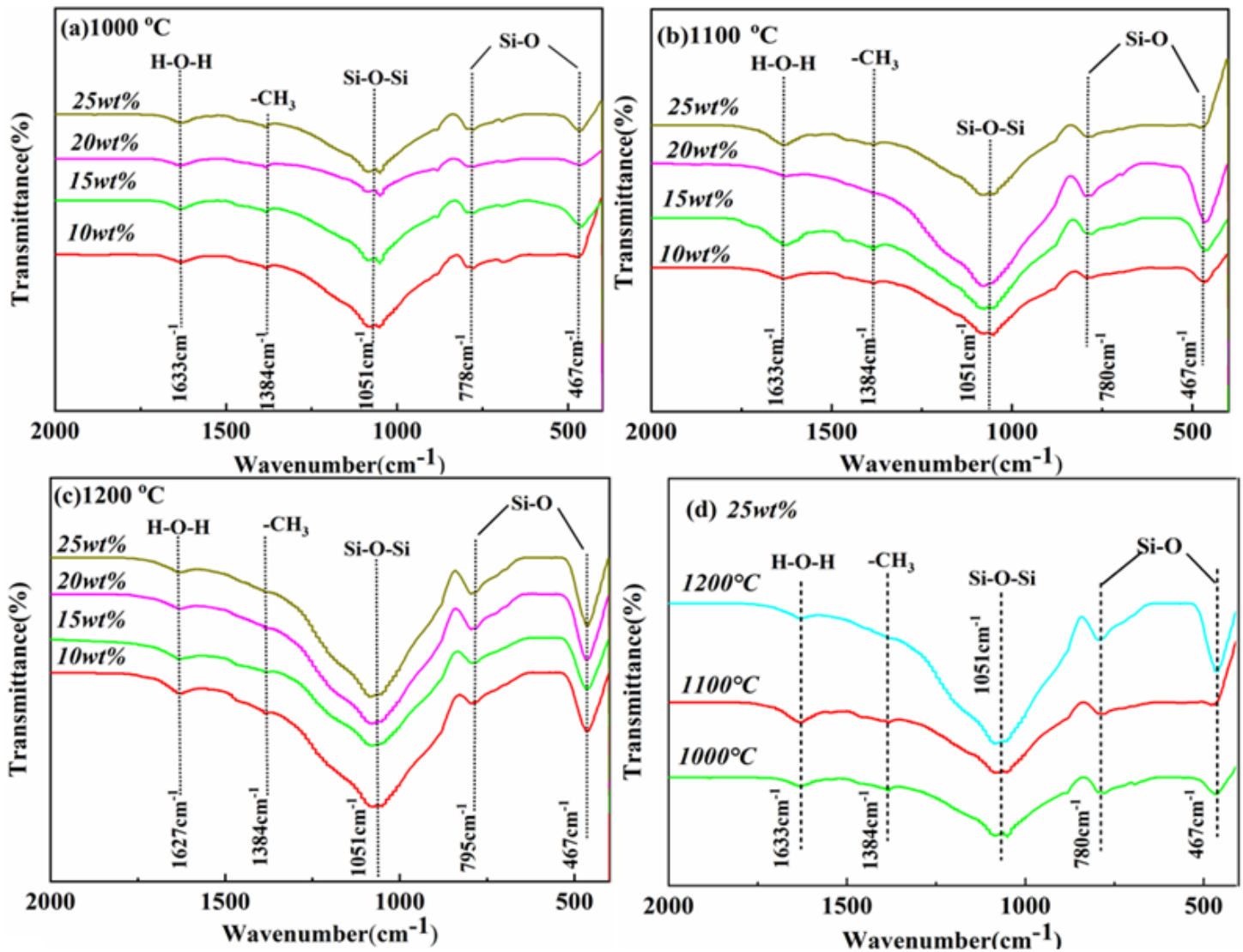


Figure 4

FT-IR spectra of samples with 10 - 25 wt % Nd_2O_3 concentrations at different temperatures

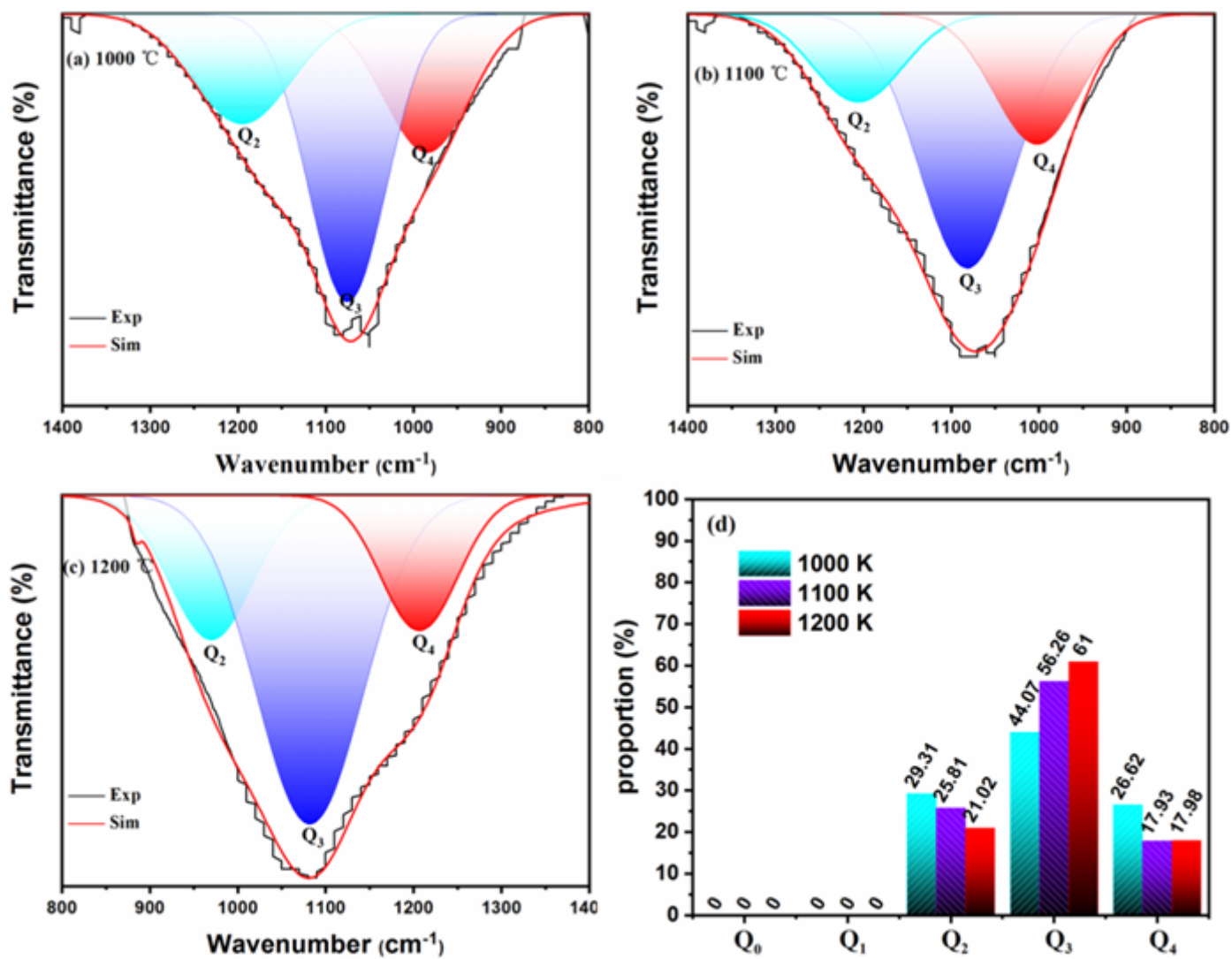


Figure 5

Q_n species of 25 wt % Nd₂O₃ doped soils at different temperature.

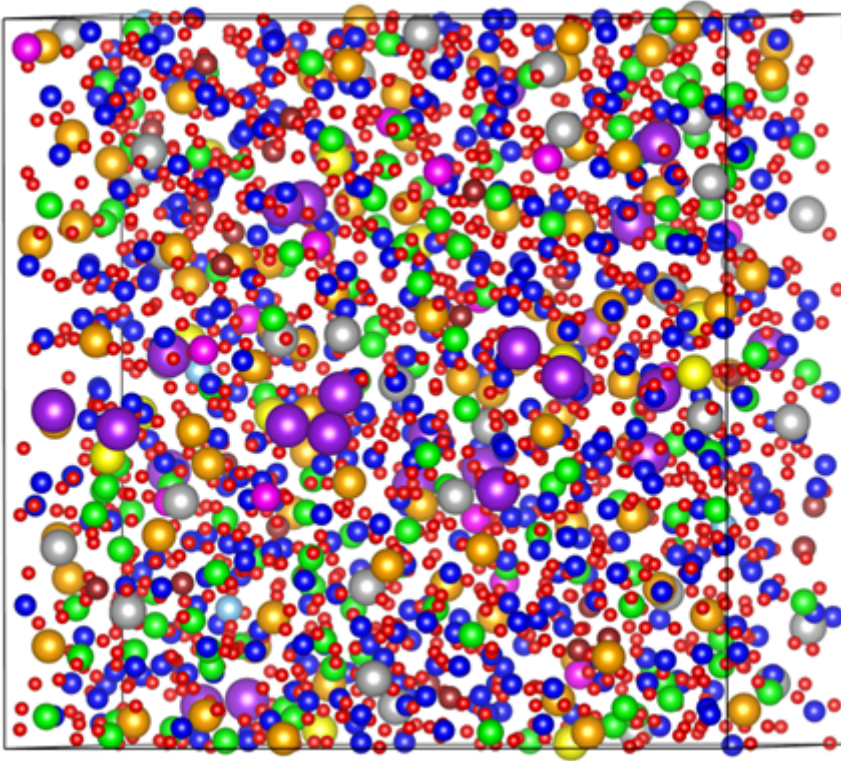


Figure 6

Simulated structure of 25 wt % Nd₂O₃ doped sintered soil. Colors (atoms) designation: orange (Nd), red (O), skyblue (Ti), yellow (Na), purple (K), magenta (Mg), brown (Fe), gray (Ca), blue (Si), and green (Al).

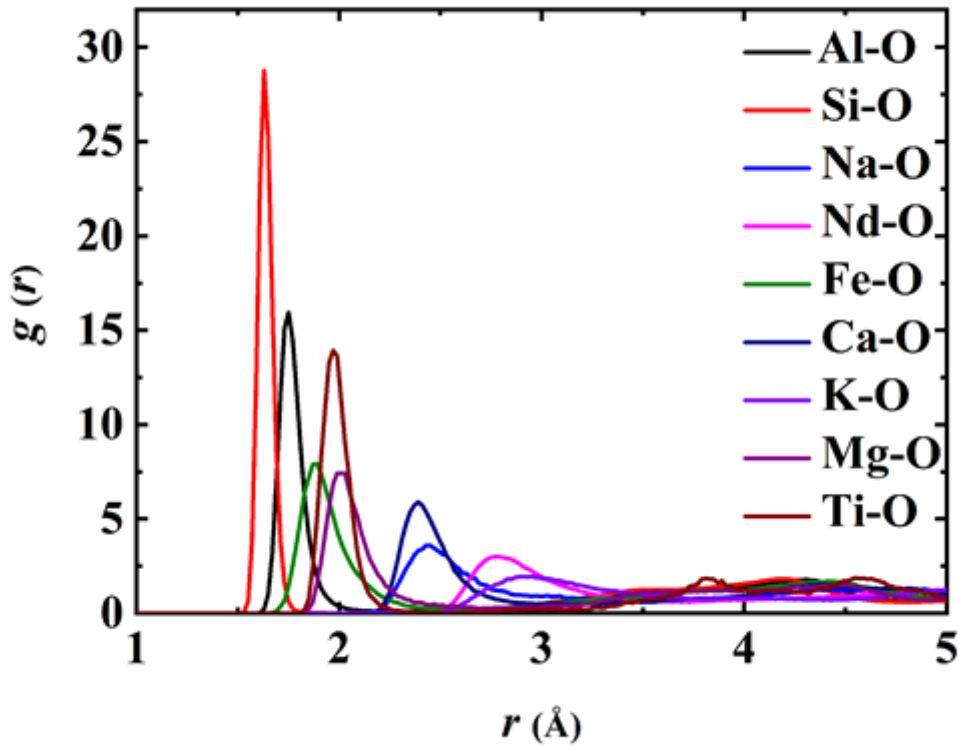


Figure 7

The simulated radial distribution function for 25 wt % Nd₂O₃ doped sintered soils

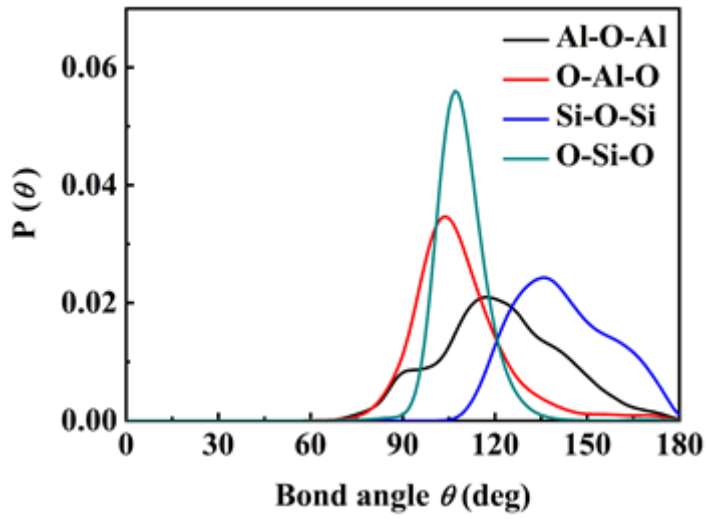


Figure 8

The simulated bond angle distributions for 25 wt % Nd₂O₃ doped sintered soils